Primljen / Received: 15.7.2025.
Ispravljen / Corrected: 26.11.2025.
Prihvaćen / Accepted: 9.3.2026.
Dostupno online / Available online: 10.5.2026.

Stress mechanism of anti-slide pile landslide in earthquake

Authors:

[1]Assist.Prof. **Feng Sun**, PhD. CE
597736357@qq.com
Corresponding authoru

[2]**Chao Jia**, MCE
519320912@qq.com

[1]Prof. **Le Zhou**, PhD. CE
zhoule 0306@126.com

[1]Prof. **Jia Yang**, PhD. CE
sydxyj@163.com

[1]Assist.Prof. **Yang Qiao**, PhD. CE
771333054@qq.com

[1]Shenyang University, School of Architectural Engineering, Shenyang, China
[2]Tieling Economic Development Zone Planning and Construction Bureau, China

Original research paper

Feng Sun, Chao Jia, Le Zhou, Jia Yang, Yang Qiao

Stress mechanism of anti-slide pile landslide in earthquake

Based on the geomechanical analysis of typical examples of slope reinforcement and indoor model test analysis, this study analyses the influence of earthquakes on the dynamic response of anti-slide piles supporting gravel soil slopes under different embedment depths and soil strengths. The aim is to reveal the variation law of the earth pressure gauge value behind the pile in the embedded section of anti-slide piles with different embedment depths and seismic time histories. When the embedment depth is relatively deep or the soil strength is relatively large, it may not fully exert the retaining effect of the anti-slide pile, and the construction is difficult and may not be economical. When the embedment depth is relatively shallow or the soil strength is relatively small, the seismic resistance effect of the anti-slide pile is poor, and the supported slope is not very stable. Based on the strength reduction unbalanced transfer coefficient method, relevant research on the embedment depth of anti-slide piles is carried out. An empirical discriminant formula is established for determining the optimal embedment depth of anti-slide piles in soils of different strengths under a certain landslide thrust condition. It further reveals the specific impacts of many sensitive factors, such as the embedment depth, soil water content, and pile-soil properties, on the distribution mode of external loads, and provides a theoretical basis and relevant scientific guiding suggestions for explaining the force mechanism of its support system and research on the specific embedment depth.

Key words:
seismic action, piles for landslide stabilization, soil strength, lateral soil pressure on the pile, optimal pile depth

Izvorni znanstveni rad

Feng Sun, Chao Jia, Le Zhou, Jia Yang, Yang Qiao

Mehanizam naprezanja klizišta stabiliziranog pilotima pri potresnome djelovanju

Na temelju geomehaničke analize tipičnog primjera stabilizacije pokosa i laboratorijskih modelskih ispitivanja u radu se istražuje utjecaj potresnog djelovanja na dinamički odziv pilota za stabilizaciju klizišta u šljunkovitome tlu pri različitim dubinama ugradnje i različitim čvrstoćama tla. Cilj je utvrditi zakonitosti promjene tlaka tla iza pilota, u području njegova ukopanog dijela, ovisno o dubini ugradnje i vremenskome zapisu potresa. Pri većoj dubini ugradnje ili većoj čvrstoći tla, potporni učinak pilota ne mora biti u cijelosti iskorišten, a izvedba može biti složenija i ekonomski nepovoljnija. S druge strane, pri manjoj dubini ugradnje ili manjoj čvrstoći tla, učinkovitost stabilizacije pri potresnome djelovanju nedostatna je, pa ni stabilnost pokosa ne zadovoljava. Na temelju metode smanjenja čvrstoće i metode prijenosnoga koeficijenta neuravnoteženog potiska provedena je analiza dubine ugradnje pilota za stabilizaciju klizišta. Dodatno se razjašnjava utjecaj osjetljivih čimbenika kao što su dubina ugradnje, vlažnost tla te svojstva sustava pilot-tlo na raspodjelu vanjskih opterećenja. Rezultati daju teorijsku osnovu i smjernice za tumačenje mehanizma djelovanja stabilizacijskog sustava te za određivanje potrebne dubine ugradnje pilota.

Ključne riječi:
potresno djelovanje, piloti za stabilizaciju klizišta, čvrstoća tla, bočni tlak tla na pilot, optimalna dubina ugradnje pilota

1. Introduction

Anti-slide piles are commonly used for controlling landslides. Because of the strength difference between different gravel soils and landslides and the particularity of the random load of ground motion, research on the internal-force change law and pile-soil reinforcement effect of anti-slide piles under earthquake action has become very complicated. According to the retrieved literature [1–4], due to the complexity of the problem and the nonlinear characteristics of rock and soil, performing physical model tests and numerical verification by means of seismic and numerical simulation of a shaking table is necessary. This study focuses on geomechanical analysis of typical examples of slope reinforcement, aiming at the interaction between anti-slide pile and landslide and its stress mechanism under earthquake load. By means of numerical simulation and indoor model test, this study analyses the influence of earthquake on the dynamic response of anti-slide pile supporting gravel soil slopes under different embedment depths and different soil strengths. These analyses reveal the variation law of the earth pressure gauge value behind the pile in the embedded section of anti-slide piles with different embedment depths according to the seismic time history. This study uses physical model tests, numerical simulation data, and the strength reduction dynamic analysis method to establish the interaction calculation model and empirical discriminant of embedded depth h with soil strength design value cohesion c and internal friction angle φ. Based on the strength reduction unbalanced transfer coefficient method, relevant research on the embedment depth of anti-slide piles is carried out. Through the selected gravel soil landslide, the influence of the soil strength on the embedded section is studied, and the optimal embedment depth of the anti-slide piles in soils with different strengths under certain landslide thrust conditions is determined. Furthermore, an empirical discriminant formula is established for the optimal embedment depth of anti-slide piles in gravel soil.

In the era of digitalisation and informatisation, computer development is rapid, and the advantages of numerical simulations are becoming increasingly evident. In the field of geotechnical engineering, the nonlinear finite element method can comprehensively reflect the mutual coupling effect between piles, the soil between piles, and their nonlinear characteristics, and can consider various distribution situations of different media, such as piles and the soil between piles. It is superior for analysing the influence of various factors influencing the interaction between piles and soil [5]. Using the finite element method to simulate the stress and deformation behaviour of anti-slide piles and serving as an auxiliary tool for the design and construction of anti-slide piles has good application prospects. Owing to the complexity of the composition of geotechnical materials and the nonlinearity of constitutive relations, as well as the complexity of complex and variable load applications and boundary conditions, achieving these using analytical methods is impossible. These numerical advantages have been verified many times in practice. Internationally, numerical simulation analysis methods are typically used to provide a basis for engineering examples and have become an important and effective method for slope engineering calculations [6]. Currently, there are significant challenges in analytical methods. Common methods, such as the p–y spring method and classical limit equilibrium method, have certain disadvantages. Taking the representative gravel-soil landslide in the Nanwen area of Yunnan as a model for comparison indicators, numerical advantages can be observed. In this study, the mean absolute error (MAE), root mean square error (RMSE), and coefficient of determination (R^2) were used to evaluate a slope anti-slide pile support model. The MAE is the average absolute deviation between the predicted and true values, reflecting the accuracy of the prediction; the closer the value is to 0, the higher the coincidence degree between the predicted value and the true value. The RMSE reflects the dispersion degree of the predicted value relative to the true value; the closer its value is to 0, the smaller the average deviation amplitude of the predicted value, and the better the model performance. R^2 describes the ability of the model to explain data fluctuations, and its value is closer to 1 [7].

The nonlinear finite element analysis shows the best performance in terms of computational performance (Table 1). The mean absolute error is 0.072 mm, the root mean square error is 0.097 mm, and the coefficient of determination reaches 0.9981. The percentage deviation of the designed embedment depth h and the percentage deviation of FS are 7.09 % and 6.84 %, respectively. Compared with other analytical methods, the nonlinear finite element analysis model significantly improves the computational accuracy and precision, indicating its superiority in the support of anti-slide piles for landslides.

2. Establishment of a geomechanical model of a typical example

A typical example is the Nanwen landslide, located on a south-inclined slope near the K123+920 – K123+950 section of the Wentian Highway in Wentian Town, Malipo County, Yunnan County. The average longitudinal length of the landslide is about 110.00 m, the average lateral width is about 40.00 m, the area is about 4400.00 m^2, the average thickness is about 18.70 m, and the volume is about 4.3 × 104 m^3, which is a typical medium-sized gravel landslide.

Table 1. Experimental results of commonly used methods

Method of application	R^2	MAE [mm]	RMSE [mm]	Percentage deviation of embedment depth "h"	Percentage deviation of "FS"
p–y springs	0.9976	0.084	0.111	8.14 %	7.85 %
Classical limit-equilibrium methods	0.9979	0.080	0.105	8.71 %	7.62 %
Nonlinear FE analyses	0.9981	0.072	0.097	7.09 %	6.84 %

2.1. Geomorphology

The landslide area is located in the fault cliff formed by the Wenshan-Malipo fault zone, which is nearly vertical, with a strike of approximately 310°, a height of approximately 100 m, and a horizontal distance of approximately 40 m from the landslide area. The undulating slope is approximately 22°–25°. The elevation changes between 394.00 and 461.00 m.

2.2. Formation lithology

According to surface survey and drilling data, the sliding mass thickness is 12.20 ~ 21.00 m. The landslide body is mainly composed of quaternary colluvial clay containing rubble, colluvial rubble, and a landslide accumulation layer. The sliding bed is a strongly weathered schist of the Upper Permian Wujiaping Formation.

2.3. Slope structure

The sliding direction of the landslide is about 188°, and the occurrence of bedrock stratum is 50°∠41°. The strike of the underlying bedrock stratum intersects the slope direction at a small angle.

2.4. Calculation parameters

According to the on-site large bulk density test and the indoor test results of sampling in boreholes, it was comprehensively determined that the weight of the landslide rock and soil had a natural bulk density of 20.4 kN/m^3 and saturated bulk density of 20.8 KN/m^3, and the material composition of the landslide was uneven; therefore, it was difficult to select parameters according to the test results. As per the suggestions, the design unit of the shear strength parameters of the sliding body should be cohesion c = 20.0 KN/m^2 and internal friction angle φ = 18.1. In the subsequent calculations, the shear strength parameters of the sliding body were consistent with the design recommendations [8].

The shear strength parameters of the sliding zone soil are highly sensitive to the landslide thrust and stability coefficient. The accurate determination of their values is key to ensuring the reliability of the calculation results and has a significant impact on pile design. The selection of various physical and mechanical property indices of the sliding zone soil should be based on the situation of the sliding mass (landslide type, genesis). Accordingly, the method of geotechnical tests or back-calculated parameters should be used, and after comparing with empirical data, the indices should be analysed and selected. The selected parameters should preferably reflect the actual values when the sliding mass is in a limit equilibrium state. For soil landslides, although the actual parameter values of undisturbed sandy soils can be accurately obtained through triaxial tests in the laboratory, obtaining the actual values of cohesive soils is difficult because of various influences, such as disturbances, and the indoor test values are generally not directly adopted. For landslides formed by the softening of structural planes caused by groundwater, the parameters should be determined by combining back-calculated values with expert experience. When the landslide is in the limit equilibrium state, the water content at the sliding zone (plane) is relatively large, generally close to the saturated state, and the water content in the sliding mass is inconsistent with that in the sliding zone; therefore, the c and φ values of the sliding zone are smaller than those in the sliding mass. If the c and φ values of the sliding zone soil are determined according to the indoor geotechnical test values in the sliding mass, they will be larger than the actual values. When using the indoor test values of the sliding zone soil to determine the c and φ values, due to excessive disturbance of the sliding zone soil during sliding, the c and φ values are smaller than the actual values. Therefore, the indoor geotechnical test values of such landslides are only suitable as references for determining the parameters. Therefore, to select the sliding zone parameters for this typical example, the test results should be combined with the back-calculated results and expert experience [9].

According to the divide-and-conquer principle, the main force direction of the third or more sliding bodies (Figure 1) on the fourth sliding body is horizontal, and the sliding thrust is relatively small. The Nanwen gravel landslide is a combination of upper and lower landslides; therefore, it it should be supported separately in engineering construction; that is, a first-class supporting structure should be set at the front edge of the third sliding body. In this study, only the landslide was removed to establish the model in the calculation described in the following sections.

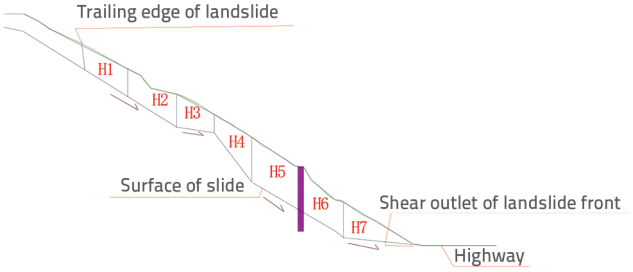

Figure 1. Zoning of calculation section of landslide

3. Physical model test

3.1. Similarity criteria to be satisfied in model experiments

According to the similarity criterion, during the simulation of landslides through model tests, the physical quantities to be satisfied are mainly general geometric, dynamic, and kinematic similarities [10]. Typically, in geomechanical model tests, formula (1) for similarity criteria should be satisfied, Eq (1):

$$\left.\begin{aligned} &\frac{C_\sigma}{C_r C_l} = 1 \\ &C_u = C_\varepsilon = C_f = C_\phi = 1 \\ &C_\sigma = C_E = C_c = C_\tau \\ &C_\delta = C_l \end{aligned}\right\} \quad (1)$$

where C_σ is the stress similarity constant, C_l is the geometric similarity constant, C_γ is the unit weight similarity constant, C_μ is the Poisson's ratio similarity constant, C_α is the strain similarity constant, C_f is the friction coefficient similarity constant, C_φ is the internal friction angle similarity constant, C_E is the elastic modulus similarity constant, Cc is the cohesion similarity constant, C_τ is the shear strength similarity constant, and C_δ is the displacement similarity constant [11].

3.1.1. Determination of similarity ratios

Based on the research purpose and similarity theory, in the model test of the Nanwen landslide, the structural phase test of materials and the similarity of mechanical (including dynamic) characteristics were adopted as the basic conditions for the experiment. Taking the axis of the Nanwen landslide as the reference axis of the experiment and a 0.5 m wide strip as the research object, the relevant geometric conditions, such as slope length, slope gradient, and slope shape, were similar in the experiment. Considering the simulation range, experimental model, experimental platform conditions, and other related factors, the geometric scale ratios of the experiment were taken as $C_l = 50$ and $C_r = 1$ [11].

In this study, microconcrete parameters were adopted from the relevant literature [8]. Microconcrete is a type of concrete composed of several fine aggregates as basic materials in a certain mix ratio. Based on the experiment, we determined that, the mechanical properties of the prototype concrete material were similar to those of microconcrete. The shape of the anti-slide model pile of microconcrete could be made similar to that of the prototype. Although the anti-slide model pile of micro-concrete was composed of two materials, there was a good similarity between the model pile and the prototype pile of micro-concrete in the elastic working stage because the mechanical properties of the two materials were very close to those of the corresponding prototype materials. According to the similarity criterion $C_\gamma C_l / C_\sigma = 1$, comprehensively considering the simulation range of the experiment and platform conditions and other factors, the geometric scale ratio $C_l = 1/30$ and $C\gamma = 1/1$ were taken. Where $C\gamma$, C_l and $C\sigma$ are the volume force similarity constant, geometric similarity constant, and stress similarity constant, respectively. Similar models that satisfy all of these requirements are extremely difficult to obtain in actual experiments. In actual experiments, only a few of the main similarity criteria were satisfied. This experiment only developed a plane stress model, satisfying the main similarity ratios that could be realised in actual experiments such as C_l, C_σ, C_γ, C_{Rc}, C_τ and C_φ. etc. Therefore, based on meeting the above similarity requirements of actual experiments:

1. $C_\sigma = 1/30$ that is, the stress on the model was 1/30 of the prototype stress in actual experiments
2. $C_q = C_l = 1/30$, that is, the distributed line load on the model was 1/30 of the prototype [11].

The sliding mass used a landslide in a loose state as the material. Under the action of the seismic force and the weight of the sliding mass, a downward sliding force was generated along the landslide. The measured unit weight of the sliding mass composition in the loose state was 20.2 kN/m³, the internal friction angle was 29.0°, and the cohesion was 18.0 kPa. As newspapers have good water absorption and water retention properties, they were used as the specific contact surface of the weak structure. The contact surface could be regarded as a sliding contact surface, and its friction coefficient was finally determined to be 0.21 through experimental tests. To stabilise the landslide, especially for studying the materials below the sliding surface, the method of layered compaction was adopted; finally, it was compacted to a dense state and hardened for a period of time to achieve a certain stability. Through experimental determination, the unit weight of the sliding bed was 27.1 kN/m³, the internal friction angle was 31.0°, and the finally measured value of the cohesion was 21.0 kPa [12].

3.2. Physical model test production

3.2.1. Shaking table equipment

The shaking table equipment consisted of a tabletop, fixed base, vibrating spring, exciting motor, model box, frequency modulation device, and a take-off and landing (slope adjustment) device. Excitation force adjustment range was 0~13000 kN, frequency adjustment range was 0.5 - 50 Hz, the size of the model box was 3.5 × 0.9 m, and its dead weight was 0.22 t. Test monitoring equipment included a vibration monitor, a three-phase vibration sensor, an earth pressure gauge, a strain gauge, a total station, etc.

3.2.2. Model development

According to the similarity theory, the structural and mechanical (including dynamic) characteristics of materials are similar to the basic conditions. A 0.5 m wide strip of the Nanwen landslide axis was taken as the research object. To achieve the best test results, four groups of related mechanical tests were conducted on landslide materials composed of barite powder, quartz sand, calcium carbonate particles, and latex. The test results showed

Table 2. Mix ratio and strength tests of similar materials

Number	Similar materials	Mixing proportion	Uniaxial compressive strength [kN/m²]
1	Barite powder. Quartz sand. Calcium carbonate particles. Latex	3.2 : 3.2 : 3.2 : 0.4	56
2	Barite powder. Quartz sand. Calcium carbonate particles. Latex	4 : 3 : 2.5 : 0.5	57
3	Barite powder. Quartz sand. Calcium carbonate particles. Latex	5 : 2 : 2.5 : 0.5	47
4	Barite powder. Quartz sand. Calcium carbonate particles. Latex	5.5 : 1.5 : 2.5 : 0.5	63

Table 3. Proportion of microconcrete

Number	Material	Particle size [mm]	Mass [g]
1.	Water	-	69.59
2.	Cement	-	124.8
3.	Fine sand	0.0 - 0.5	105.4
4.	Medium sand	0.5 - 1.25	52.74
5.	Bone granule 1	1.25 - 2.0	100.0
6.	Bone granule 2	2.0 - 5.0	147.3

Table 4. Acceleration sensor conditions

Mass [g]	Sensitivity [mV/g]	Measured frequency min [Hz]	Measured frequency max [Hz]	Measurement range [g]
20	100	0.5	5000	50

that under the same test conditions, the uniaxial compressive strength of the third group of samples was the smallest, and the bulk density was higher. After drying for 36 h under natural conditions, the test results showed that the samples had properties of gravel soil. Therefore, the materials in the third group were selected for the model tests (Table 2).
According to the relevant literature [13, 14], microconcrete is made from several fine aggregates mixed in specific proportions determined by experiments. The cement grade was 425. The mix proportions of the microconcrete specimens are listed in Table 3.

3.2.3. Test content and test point arrangement

The total station was used to observe the entire process, and its value represented the change in displacement [15]. Simultaneously, the position of the relative earth pressure gauge should be conducive to observing the specific earth pressure at the corresponding position to test the change in earth pressure. Therefore, 3 earth pressure sensors were used: one in the sliding zone, one in the sliding body 1/2, and one in the embedded section of the anti-slide pile near the sliding zone. The test model and specific arrangement of the test points are shown in Figure 2. The model piles were divided into five groups of two piles each. According to the geometric-similarity criterion, the cross-sectional size of the model piles was 40 x 30 mm, and the pile spacing was 12 cm. The ratio of the model to experimental prototype was 1:50. The embedding depths of the first group to the third group were 0.2, 0.16, and 0.12 m, respectively. The sliding body thickness of the model was 0.6 m, and the sliding bed thickness was 0.3 m. For acceleration response monitoring, a column of accelerometers (A1–A6) was arranged along the axis of the model to eliminate the influence of boundary effects. The conditions of the acceleration sensors are listed in Table 4.

3.2.4. Test cond itions

According to experimental requirements, the seismic wave parameters should always remain the same [16]. According to the Code for Design of Concrete Structures [8], for earthquakes with an intensity of more than 7 degrees, the seismic cross-section for frequent earthquakes must be carried out. Therefore, the experiment in this study was performed according to the requirements for seismic intensity of 7 degrees. Its horizontal input direction was consistent with the long side of the model box and perpendicular to the short side, that is, along the direction of the slope. Absorbing measures were taken on the two walls in the main vibration direction, that is, a 20.5 mm thick polystyrene foam layer was lined on the left and right walls of the model box to reduce the "model box effect". Table 5 provides information on various test conditions, such as the seismic wave parameters.

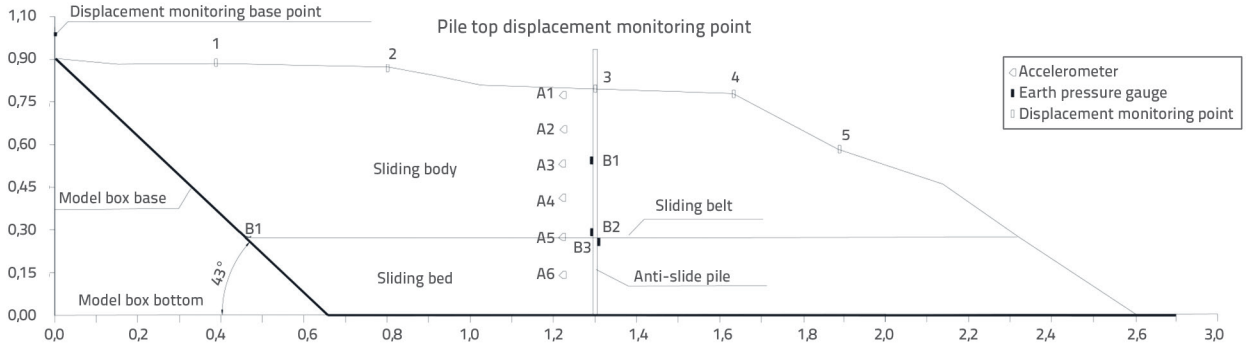

Figure 2. Physical model used in the test

Table 5. Test conditions

Sensitivity	Vibration frequency [Hz]	$A_{X,max}$ [g]	$A_{Y,max}$ [g]	Sampling rate [Hz]
0,108	5,5	0,30	0,28	1000

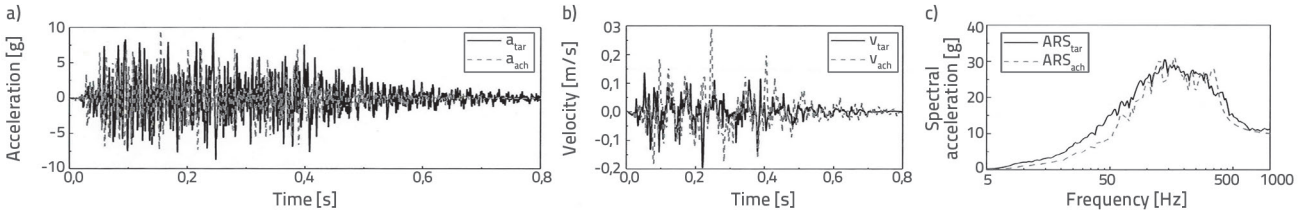

Figure 3. Comparison of tabletop and target vibrations of seismic waves: a) acceleration time history; b) velocity time history; c) acceleration response spectrum

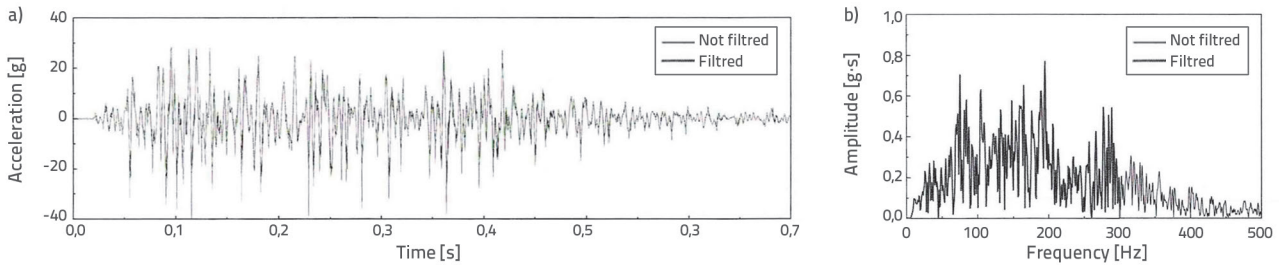

Figure 4. Comparison of tabletop vibrations of seismic waves before and after filtering: a) acceleration time history; b) acceleration response spectrum

Comparison of target acceleration and acceleration time history of seismic waves, target velocity and tabletop velocity time history, and target acceleration and acceleration response spectra is presented in Figure 3. The figure reveals that through vibration control, the peak acceleration of the tabletop of the seismic wave is consistent with the peak value of the target acceleration; the peak error is within 6.7 %, and the area error is within 32.3 %. The tabletop accelerations represent the peak and valley values of the target acceleration. By comparing the vibration control errors, the error decreases with an increase in the vibration amplitude. The acceleration response spectrum of the tabletop fits well with the target acceleration response spectrum and exhibits common characteristics with other frequency bands [15].

Acceleration time history and response spectrum of the waveform output on the tabletop before and after filtering are shown in Figure 4 [16]. Signal components with frequencies higher than 300 Hz were not considered, because they exceeded the working range of the shaking table. Figure 4 depicts that reasonable filtering does not affect the evaluation of the vibration control effect.

Using the acceleration time history measured by accelerometers arranged at different depths during the test, the shear stress and shear strain at different depths of the site were calculated, and the stress-strain relationships at different depths were obtained. The shear stress at the depth of a given accelerometer can be calculated using the following Eq (2):

$$\tau(z_i) = \tau(z_{i-1}) + \rho \frac{(ii_{i-1} + ii_i)}{2} \cdot z_{i-1}, \quad i = 2,3,\cdots \tag{2}$$

For the solution of the shear strain, the acceleration signal is first integrated twice in time to obtain the displacement signal, and a second-order approximation is then used to obtain the average shear strain near this depth, according to the following Eq (3):

$$\gamma(z_i) = \frac{\left[(u_{i+1} - u_i)\frac{(z_i - z_{i-1})}{(z_{i+1} - z_i)} + (u_i - u_{i-1})\frac{(z_{i+1} - z_i)}{(z_i - z_{i-1})}\right]}{(z_{i+1} - z_{i-1})} \tag{3}$$

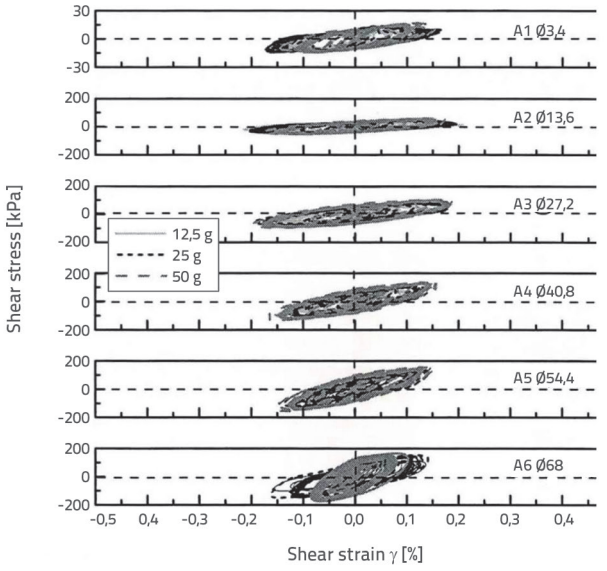

Figure 5. Shear stress-shear strain hysteresis loops of soil at different depths

As shown in Figure 5, the prototype stress-strain hysteresis loops revealed under different accelerations fit well, indicating the feasibility of revealing the prototype using the unequal stress similarity law of the vibration table and equal shear strain.

3.2.5. Analysis of amplification effect

Considering that the stress-strain relationships of the prototypes simulated under acceleration were similar, the test results under 50 g were used to analyse the amplification effect of the slope. The amplification effect of the slope was evaluated using an amplification coefficient, and the amplification coefficient was defined as the peak ground acceleration (PGA) or peak ground velocity (PGV) at different depths.

As shown in Figures 6 and 7, under the same vibration, the acceleration and displacement amplification coefficients exhibit an amplification trend from the bedrock to the slope crest and reach a maximum at the slope crest. The acceleration amplification coefficient could reach 2.4 at the slope crest, while the displacement amplification coefficient could reach 2.7 at the slope crest. The acceleration amplification coefficient first increased and then decreased with increasing vibration intensity, whereas the velocity amplification coefficient always increased with increasing vibration intensity. Under a large vibration of 0.3g, the acceleration amplification coefficient showed a decreasing trend, and the velocity amplification was more significant. This is because the stress-strain relationship of rock and soil materials is nonlinear, and the material stiffness decays under large strains.

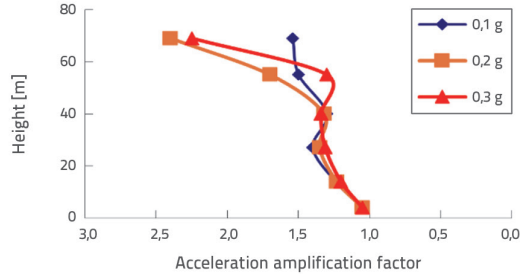

Figure 6. Acceleration amplification coefficients at different depths

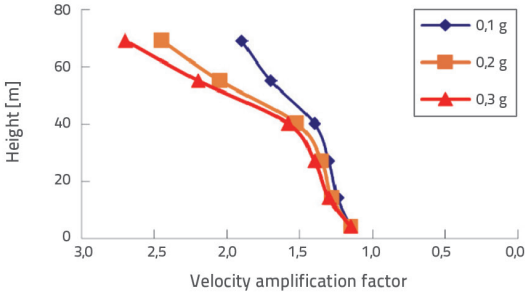

Figure 7. Velocity amplification coefficients at various depths

3.2.6. Arias intensity and peak acceleration of earthquake vibration intensity

Earthquake accumulation continuously increases soil density, thereby enhancing the stiffness and strength of gravelly soil [15].

Therefore, the relationship between the earthquake vibration intensity and material density was analysed. As can be seen from Figure 8, the Arias intensity (I_a) and peak acceleration (a_{max}) are selected to characterise the earthquake vibration intensity. Arias (1970) proposed that the Arias intensity represents the amount of energy absorbed per unit of soil mass during an earthquake. The I_a is defined as Eq (4):

$$I_a = \frac{\pi}{2g}\int_0^{t_a} a^2(t)\,dt \tag{4}$$

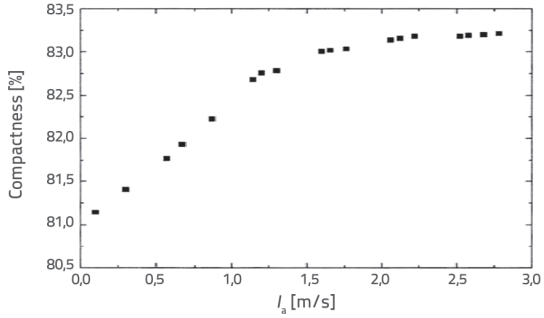

Figure 8. Relationship between density and Arias intensity (test values)

The small-strain shear modulus G_{max} of the soil is a parameter that comprehensively reflects the properties of the soil, mainly determined by the effective stress and void ratio, and can comprehensively reflect the structural characteristics of the soil [16]. The relationship between the small-strain shear modulus and degree of compaction of the fill body (Figure 9) was fitted according to the formula to obtain the fitting parameters.

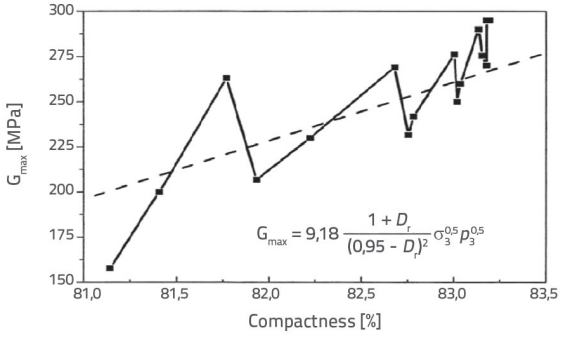

Figure 9. Relationship between small-strain shear modulus and density

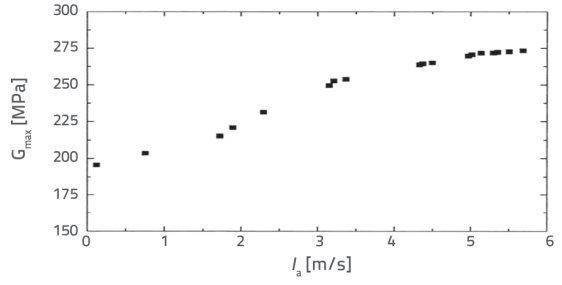

Figure 10. Relationship between small-strain shear modulus and Arias intensity (obtained by fitting)

Table 6. Quantitative indicators of the gravel soil under different conditions

State of gravel soil	Water content "w" [%]	Saturation "S_r" [%]	Unit weight "γ" [kN/m³]
Moist state	13.2	64.7	21.1
Natural state	8.6	39.1	19.3
Dry state	4.8	21.1	17.4

By combining the relationship between the degree of compaction and the Arias intensity established at the beginning of this section, the relationship between the small-strain shear modulus and Arias intensity of the fill body can be obtained, as shown in Figure 10.

4. Stress analysis of anti-slide pile and slope

4.1. Influence of soil strength

The soil with natural water content in this study refers to the slope in a typical example, which is in the natural state without rainfall; the wet soil refers to the soil with water content under the condition of heavy rainfall or a high groundwater level, and the dry soil refers to the water content when the soil is dry [16, 17]. The quantitative indicators of gravel soil in different states are listed in Table 6.

As shown in Figure 11, with a continuous input of the earthquake load, the change in the pile-top displacement increases gradually. Under the same earthquake load, if the values of soil C and φ are different, the corresponding pile top displacement is also different. On the contrary, the values of C and φ in the slope of dry soil are the largest, while the weight of soil is the smallest, and the displacement change of pile top is the largest under the same vibration condition; the situation of soil with higher water content is just the opposite. This further indicates that the higher the degree of cementation and the greater the cohesive force, the stronger the ability to resist the constraint of the sliding piles. Under the same load, the inflexion point of the sliding of dry soil was also significantly advanced. The seismic effect is not only related to the embedded depth of anti-slide piles but also significantly influences soil strength. Improving the soil strength of a slope is also an important factor that must be considered in the actual design.

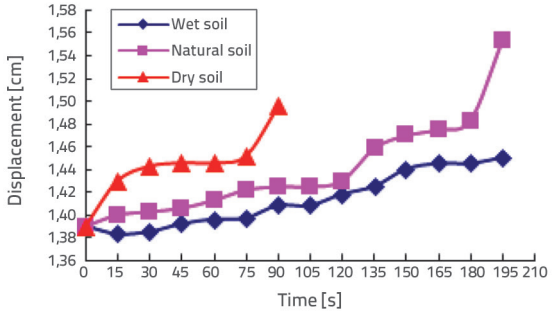

Figure 11. Variation curve of pile top displacement with vibration time for different soil strengths

Figure 12 shows that as the slope of the soil strength decreases, the displacement at the top of the slope increases gradually and finally becomes a smooth curve. Within the first 50 s, the displacement and deformation of the top of the slope were the largest and, of course, the most intense. The experimental phenomenon showed that the soil changed from a loose state to a dense state. Even for wet soil, the deformation tended to increase overall because of the change in water content during vibration. However, except for dry soil, the displacement at the top of the slope had no inflexion point. Owing to the drying of the dry soil, the friction between the soil particles also reduced. With earthquake damage to the soil behind the pile, the anti-slide pile and the soil behind the pile are expected to have inflexion points and slide as a whole, thereby further driving the dry soil and sliding further.

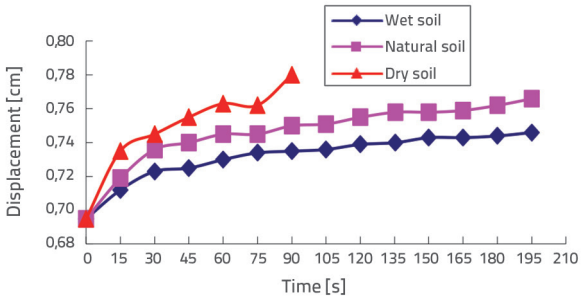

Figure 12. Displacement of point No.1 on the downhill top with different soil strengths varied with vibration-time variation curve

Figure 13 shows that both wet and dry soils undergo bulging deformation and are ultimately destroyed during the earthquake; the only difference lies in the time scale. During the early stages of the earthquake, the deformation of the soil arch is relatively large. In particular, for wet soil, the displacement and deformation of the soil in the middle of the pile finally stabilise in approximately 100 s, which is influenced by the soil arch in the middle of the pile. The water content and porosity of the soil change constantly before the earthquake, but are always relatively stable during soil arching due to earthquakes. Therefore, the slope of wet soil may not perform its intended retaining function, and constructing it in practical engineering is difficult and may be uneconomical. In contrast, the slope of dry soil is easily destroyed owing to external changes, and the seismic effect is poor. Notably, while controlling soil strength, other related factors need to be considered comprehensively so that the best economic effect can be achieved finally.

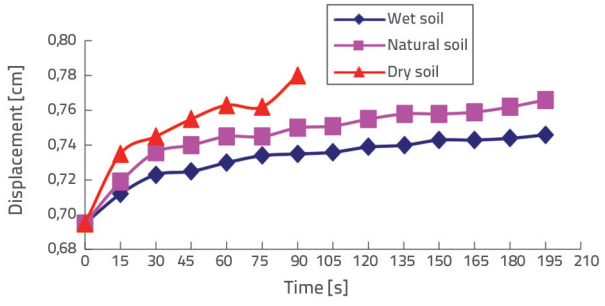

Figure 13. Displacement of point No.1 on the downhill top with different soil strengths varied with vibration-time variation curve

4.2. Influence of pile top displacement and soil pressure behind the pile in the embedded section under different embedded depths

This study focused on a selected gravel-soil landslide to investigate the influence of soil strength on the embedded section, determine the optimal embedment depth of anti-slide piles in soils with different strengths under certain landslide thrust conditions, and establish an empirical discriminant formula for the optimal embedment depth of anti-slide piles in gravel soils [17]. The evaluation of whether the embedment depth in this study was too shallow, moderate, or too deep was based on the discriminant formula obtained experimentally. Through the analysis of model tests and the similarity of landslide deformation reflected by excessively shallow, appropriate, and excessively deep embedment depths in actual projects and relevant literature [18], the accuracy of the experiments and verification of actual projects were further demonstrated. The following analyses were conducted on the anti-slide pile-supported slopes with different embedment depths.

Figure 14 shows that under the action of seismic loads, the displacement at the pile top increases with a decrease in the embedded depth, and the pushing of the anti-slide pile also increases. When the embedded depth is 20 cm, the displacement curve at the pile top of the anti-slide pile is approximately a straight line, and there is no inflexion point. The anti-slide pile and slope body do not undergo damage or large sliding, indicating that the anti-seismic effect of the anti-slide pile is good; however, there is inevitably a certain degree of waste. The deformation curves with embedded depths of 16 and 12 cm reveal that both curves have inflexion points of varying degrees, and these points can precisely serve as characteristics of the damage to the embedded section of the anti-slide pile and the loss of the anti-slide effect of the anti-slide pile. When the embedded depth is 16 cm, two inflexion points appear at 120 and 180 s of vibration. These are the time points when the soil around the anti-slide pile and the soil in front of the pile suddenly collapse; additionally, at this time, the embedded section of the anti-slide pile has been damaged, and the anti-slide pile has completely lost its anti-slide function. When the embedded depth is 12 cm, the deformation curve at this time is approximately an inclined straight line, indicating that the embedded section of the anti-slide pile has been continuously pushed, and the soil in the embedded section has been continuously damaged, indicating the instability of the soil in the embedded section. This is clearly not conducive to the anti-slide pile playing an anti-slide role. In the last 15 s of vibration, the soil in front of the pile and the anti-slide pile undergo overall sliding along the sliding surface, and the sudden displacement is 2.5 times that of the anti-slide pile with an embedded depth of 16 cm. In summary, when the embedded depth was 12 cm, the anti-seismic effect of the anti-slide pile was poor, and the supported slope body was unstable. Therefore, when the embedded depth was small, the anti-seismic support effect of the anti-slide pile was poor. Therefore, a reasonable selection of the embedded depth is both economical and conducive for the anti-slide pile to provide the anti-seismic support effect, and it has important research significance [18].

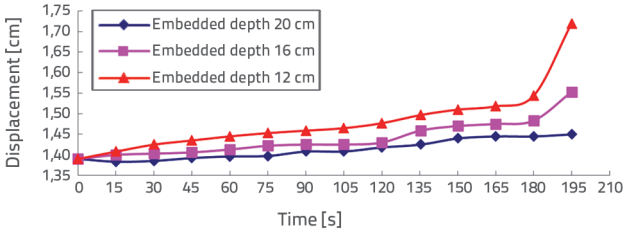

Figure 14. Displacement-time curves of pile tops with different embedment depths under vibration

Figure 15 shows that, with an increase in the embedded depth, the earth pressure values generally decrease. In particular, when the embedded depth was 12 cm (relatively shallow), the earth pressure was relatively high.

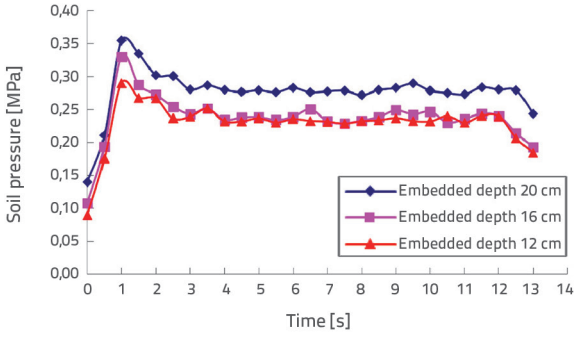

Figure 15. Variation in earth pressure gauge values behind piles in embedded sections with seismic time history at different embedded depths

When the embedded depth was 20 (relatively deep) or 16 cm (relatively appropriate), the earth pressures did not differ significantly. Within a certain embedded depth, the earth pressure reached a certain value, and increasing the embedded depth had little effect on the earth pressure. This indicates the existence of a certain stress and deformation zone for the earth pressure behind the piles in the embedded section, and that the stress and deformation zones have a certain range. Beyond this range, the anti-sliding effect of the anti-slide pile is not obvious, and

Table 7. Physical and mechanical parameters of different materials

Material	Severe "γ" [kN/m³]	Elastic modulus "E" [MN/m²]	Poisson's ratio "ν"	Internal friction angle "φ" [°]	Cohesive force "c" [kN/m²]
Sliding body	20.4	16.0	0.32	18.1	20.0
Sliding surface	17.7	15.0	0.36	18.71	15.1
Sliding bed	23.8	2100.0	0.25	26.0	210
Pile	25.0	30000.0	0.2	Considered elastic material	

increasing the embedded depth at this time is somewhat wasteful. When the embedded depth is 12 cm (relatively shallow), owing to the insufficient embedded depth and unchanged thickness of the sliding mass, under the action of the same seismic load, the overall thrust on the embedded section changes little, resulting in a relatively larger distribution of earth pressure behind the piles in the embedded section; thus, the earth pressure is relatively large, and it is relatively easy to damage [18].

5. Numerical simulation experiment

5.1. Establishment of numerical simulation experimental model

The numerical calculations and experimental models in this study correspond to a typical example of a Nanwen gravel landslide. Owing to the limitations of the experimental conditions, the similarity of the experimental model was not as good as that of the numerical calculation model in terms of the corresponding typical example. The similarity of the support landslide in the numerical model corresponding to a typical example was relatively easy to achieve; therefore, the similarity implementation was better than that of the model test. The height of the gravel landslide at the typical point was taken as 58.0 m, the width of the pile cross-section was 1.5 m, the height was 2.0 m, the longitudinal soil of the pile was taken 7.0 m away from the centre of the pile, the longitudinal pile spacing was 6.0 m, the soil thickness above the sliding surface at the pile location was 20.0 m, and the buried depths of the sliding bed were taken as 10.0, 9.0, 8.0, 7.0, and 6.0 m. The large-scale finite element commercial software ANSYS was used for the calculations, and the sliding zone and anti-slide piles were simulated using the contact elements. Considering both the interaction between the pile and soil and the influence of the confining pressure on the failure characteristics, the non-separating contact elastoplastic finite element algorithm could obtain information on the dynamic deformation and failure process of landslide and anti-slide piles from aspects such as stress, strain, sliding state, and dynamic displacement, and could reveal the seismic reinforcement mechanism of anti-slide piles from a mechanical aspect [19]. To analyse the seismic dynamic displacement of the slope, the anti-slide piles and landslide soil were simulated using the 4-node PLANE42 element provided in ANSYS. To analyse the bending moment and shear force of the anti-slide piles, the gravel soil was simulated using the 4-node plane element PLANE42. The anti-slide piles were simulated using the beam element BEAM3. The cross-sectional area, moment of inertia, etc., of the pile could be defined in their corresponding real constants because these elements could reveal the axial force, shear force, bending moment, etc. The initial values of the calculation parameters of the sliding body, sliding zone, and sliding bed (in the state of no groundwater action, referred to as the natural state), and the calculation parameters of the anti-slide piles were determined through comprehensive analysis by methods such as field and laboratory tests and back-calculation of mechanical parameters (the specific parameters are listed in Table 7). The shear strength parameters of the sliding zone soil are highly sensitive to the stability coefficient and landslide thrust; accurately determining their values is key to ensuring the reliability of the calculation results and has a significant impact on the design of the piles. The selection of various physical and mechanical property indices of the sliding zone soil should be based on the situation of the sliding body (landslide type, origin), and should utilise geotechnical test data or the method of back-calculated parameters; the selection should be made after comparison with empirical data and careful analysis [20].

The dynamic analysis of the structure adopted the transient dynamic analysis technology. The seismic wave used was "Tianjin, China (1975) Earthquake Record", and the recording time of the Tianjin wave was 5 s, and the time interval was 0.01 s. There were

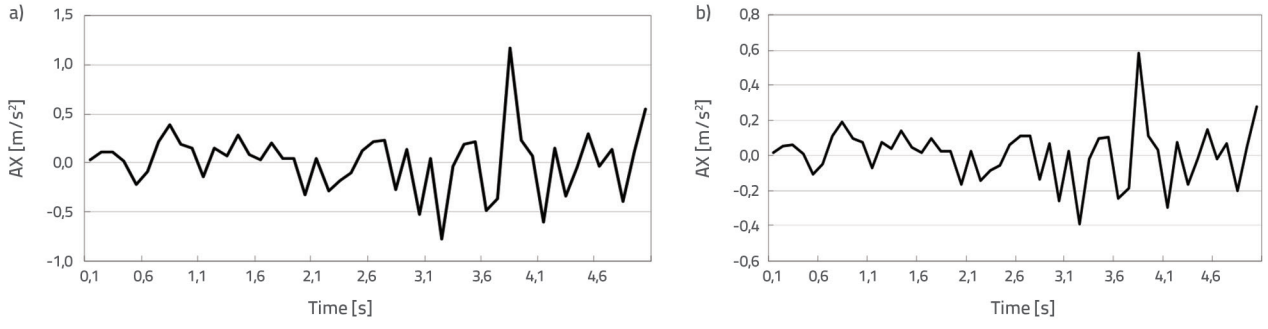

Figure 16. Time records of Tianjin earthquake wave acceleration: a) horizontal component; b) vertical component

three types of venues. Figure 10 shows the horizontal and vertical acceleration time history curves for the Tianjin wave [15].

$$\frac{a_V}{a_{V\max}} = \frac{0.125g/2}{0.7556} = 0.8114 \quad (5)$$

The Tianjin wave record was multiplied by 0.8114 before use. The seismic wave data curve after sorting is shown in Figure 16.
The geometric model was based on the geological engineering profile of the slope. Under the premise of an unchanged formation structure, the boundary dimensions of the model were appropriately extended to achieve accurate simulation calculations [21]. Viscous artificial boundaries were adopted for the side and bottom surfaces to constrain the horizontal displacements $U_X = 0$ and $U_Y = 0$. Vertical and horizontal displacement constraints were applied at the lower boundary. The slope body was used as a free face for the seismic response without any constraints. To simulate real propagation accurately, the grid size of the slope model should not be greater than 1/8–1/10 of the wavelength corresponding to the highest frequency; otherwise, large errors would occur. A seismic wave was input from the bottom-surface boundary. The grid was refined at the stress concentration areas of the structure, and sparse grids were used away from the load areas [22]. The grid size was 4 m for the slope, and 2 m for the anti-slide piles, and quadrilateral elements were used for the division. Figure 17 shows the finite element calculation profile model of the slope when the embedded depth of the anti-slide pile in the Nanwen landslide is 8 m.

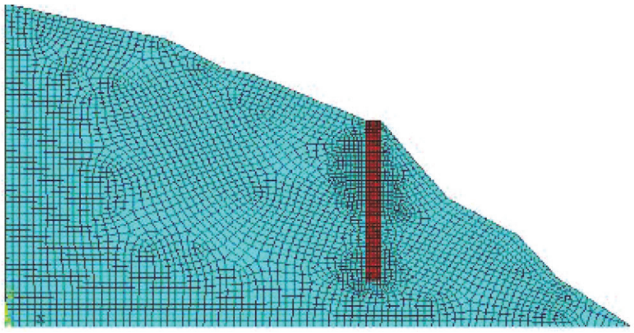

Figure 17. Profile model for calculation of the embedded depth of 8 m of the anti-slide pile in the Nanwen landslide

Rayleigh damping assumes that there is a strong correlation between the damping matrix C, stiffness matrix K, and mass matrix M in the dynamic equation of the geotechnical structure, that is, the former is a linear combination of the latter two [22]. As shown in Equation (6):

$$C = \alpha C + \beta K \quad (6)$$

Where α is the damping coefficient linearly related to the mass matrix M, and β is the damping coefficient linearly related to the stiffness matrix K. The mass matrix component in the Rayleigh damping matrix is similar to the damper between each connection node and the ground, while the stiffness matrix component is a damper. The mass matrix component, stiffness matrix component, and frequency are all related, and the dynamic response has nothing to do with damping. In order to approximately simplify the damping matrix, appropriate minimum damping ratios and frequency parameters must be set. Therefore, to determine the minimum damping ratio, dynamic calculations need to be carried out in the elastic stage of the geotechnical body, and it must be based on the damping ratio-strain amplitude curve obtained in the dynamic experiment. The general value range of the minimum damping ratio is 2 %–5 %. In order to obtain the minimum frequency parameter, undamped calculations of the elastic geotechnical body need to be carried out. However, for simple geotechnical dynamic constitutive models, undamped free vibration calculations can be performed. Filtering is a means of signal processing that can effectively suppress and prevent the influence of interference on the calculation results. Filtering the seismic wave spectrum mainly filters waves with higher frequencies in the spectrum. In contrast to other waveforms, the time history of seismic waves is often very short, and the acceleration easily reaches its peak value. The grid size needs to be divided very finely, resulting in a significant increase in the calculation time, and a high-performance workstation needs to be configured to effectively perform numerical calculations. Referring to the inverse law of wavelength and frequency, if high-frequency seismic waves can be filtered out and low-frequency seismic waves with longer wavelengths remain, the number of grid cells can be greatly reduced when dividing the grid model, reducing the computer usage requirements and saving time, thereby significantly improving the efficiency of the numerical simulation. The fluctuation energy of seismic waves is mainly concentrated in the low-frequency components; therefore, the key to seismic waves lies in the low-frequency waves, whereas the high-frequency component is unimportant. Filtering the high-frequency region can save time in the model calculations [22].

5.2. Determination of embedded depth based on strength reduction coefficient method

5.2.1. Basic principle of strength reduction coefficient method

The strength reduction method gradually reduces the shear strength of the slope (the shear strength of the slope is divided by a coefficient, i.e. the strength reduction coefficient, to achieve the purpose of strength reduction), until the slope reaches the critical equilibrium state, where the reduction coefficient can be regarded as the safety coefficient of the slope. The formula is as follows:

$$c' = \frac{c}{k} \quad (7)$$

$$\varphi' = \arctan\frac{\tan\varphi}{k} \quad (8)$$

c′ are φ′ are the reduced cohesion and internal friction angle, respectively.

In the calculation, the initial reduction factor was selected first, and the shear strength parameters of the soil in the embedded section of the slope were gradually reduced using Equations (7) and (8). If the program converges, the soil remains in a stable state, and then the reduction factor is increased until it does not converge. The reduction factor at this time is the stability safety factor, FS, of the slope. This method is called the strength reduction factor method [13].

5.2.2. Judgment methods and bases for slope instability

However, there are still differences in the judgment of slope failures within the academic community. Most researchers believe that the failure mode primarily manifests as the appearance of a plastic penetration zone in the slope, a sudden change, and a continuous increase in slope displacement. Using the finite element software ANSYS to simulate this process, it is manifested as a nonconvergence of the calculation and a sudden change in the number of iteration steps. There are usually three methods for determining whether a slope is unstable or damaged [23]:

- Convergence or non-convergence of numerical calculations. When using the ANSYS finite element calculation platform for numerical calculations, if the calculation process stops because of nonconvergence and the number of iterations changes suddenly, the slope can be considered unstable and damaged at this time.
- Plastic zone penetration. Previous slope instability cases reveal that if a plastic penetration zone appears, there is a high probability of slope instability and damage. Typically, plastic strain appears at the toe of the slope and extends upward until an arc-shaped penetration zone is formed. Even if the slope is not unstable or damaged, a plastic penetration zone may appear; therefore, this cannot be used as the only criterion for instability and damage, but it can be used as a basis for judging slope instability.
- Sudden change in the displacement of special points. The horizontal and vertical displacements of some special points on the slope are monitored in real time. Any sudden change in the displacement of these points is determined by monitoring the change in the displacement magnitude to judge the instability of the slope.

Table 8. Parameters after the strength reduction of gravel soil

Reduction factor	Cohesion c [kPa]	Angle of internal friction φ [°]
0.50	40.00	55.47
0.75	26.67	44.09
1.00	20.00	36.00
1.25	16.00	30.17
1.50	13.33	25.84
1.75	11.43	22.54
2.00	10.00	19.96
2.25	8.89	17.89
2.50	8.00	16.20
2.75	7.27	14.80
3.00	6.67	12.71

The above three criteria must be combined for a comprehensive judgment. First, the plastic zone criterion is used to exclude stable slopes. If a slope is unstable or damaged, it inevitably has a plastic penetration zone from the toe to the top of the slope. If there is no penetration zone, the slope can be considered stable. The first and third criteria are judged simultaneously. If there is a sudden change in the slope displacement and non-convergence in the finite element calculation, and the plastic zone penetrates from the toe to the top of the slope, the slope can be judged to have been damaged. The parameters of the gravelly soil after strength reduction are listed in Table 8.

Figure 18 shows that the horizontal displacement at the pile top decreases with an increase in the reduction factor. When the reduction factor is 2.3, the descending speed of the curve reaches its maximum value. This is the inflexion point of the curve, indicating a sudden change in the displacement at the toe of the slope. According to the third instability criterion, the slope can be considered as damaged. When the reduction factor reaches 2.75, the horizontal displacement at the top of the pile does not change, indicating that the calculation stopped. According to the first instability judgment criterion, the slope is considered damaged at this time [24].

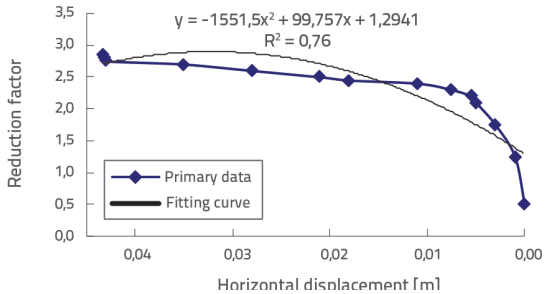

Figure 18. Variation curve of the reduction factor with horizontal displacement at the pile top

5.2.3. Determination of embedding depth under different soil strengths

Considering that the overall stability safety factor of the slope under the earthquake load may be less than 1, when the strength reduction factor method is used for analysis, the reduction factor is varies from 0.7 to 1.8, and the functional equation with a high fitting degree between the safety factor FS and the embedded depth h is obtained. As shown in Figure 19,

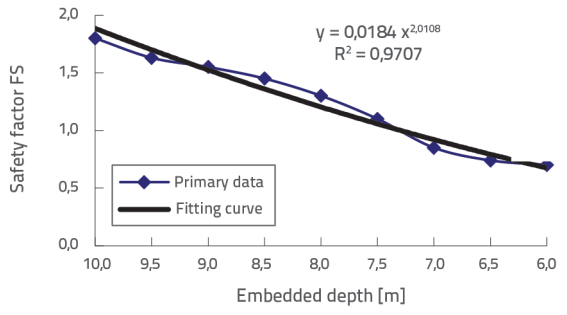

Figure 19. Relationship between the FS and embedded depth h

Table 9. 95 % confidence interval for fixed depth and FS coefficient

Embedded depth "h" [m]	FS	Lower confidence limit	Confidence upper limit
10.5	1.95	1.82	2.07
11	2.09	1.93	2.26
11.5	2.24	2.04	2.44
12	2.39	2.16	2.61

Table 10. 95 % confidence intervals of the embedded depth and internal friction angle

Embedded depth "h" [m]	Internal friction angle "φ" [°]	Lower confidence limit	Confidence upper limit
10.5	17.91	16.63	19.19
11	15.01	13.73	16.29
11.5	12.11	10.83	13.39
12	9.21	7.93	10.49

Table 11. 95 % confidence intervals of embedded depth h and cohesion c

Embedded depth "h" [m]	Cohesive strength "c" [kPa]	Lower confidence limit	Confidence upper limit
10.5	100.61	82.61	118.62
11	91.10	54.04	128.17
11.5	81.59	20.49	142.70
12	72.085	16.96	161.13

FS = $0.0184h^{2.0108}$, where the parameter is R^2 = 0.9707 [24]. The fitting range of h is 6–10 m, and the 95 % confidence intervals of the embedded depth and the FS coefficient are listed in Table 9. The curve of the relationship between the internal friction angle φ and the embedding depth h in the embedded section is shown in Figure 20. By fitting it, the functional equation of the relationship between the internal friction angle φ and the embedding depth h in the embedded section is obtained: $\Phi = 594.03h^{-1.419}$, where the parameter R^2 = 0.9773. The fitting range of h is 6 to 10 m, and the 95 % confidence intervals of the embedded depth and internal friction angle are listed in Table 10.

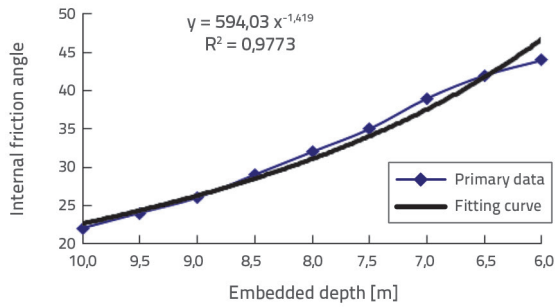

Figure 20. Relationship curve between internal friction angle φ and embedment depth h in embedded section of soil

The variation curves of soil cohesion c and embedding depth h in the embedded sections are shown in Figure 21. Fitting it, the functional equation of the relationship between soil cohesion c and embedding depth h in the embedded section is obtained: $c = 14366h^{-2.13}$, where the parameter R^2 = 0.9878. The fitting range of h is 6–10 m, and the 95 % confidence intervals of the embedded depth and cohesion C are listed in Table 11.

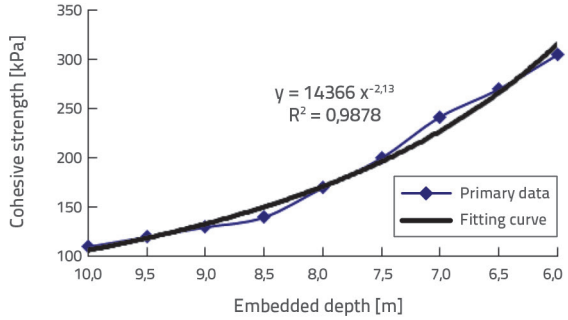

Figure 21. Relationship between soil cohesion c and embedment depth h in the embedded section

6. Embedded depth of anti-slide piles based on the strength reduction unbalanced transfer coefficient method

6.1. Derivation of the thrust formula of test landslide under seismic force

In current practical applications of landslide thrust calculations, the unbalanced transfer coefficient method is generally adopted. For typical examples and the characteristics of the slip surface

in this test, which is a broken line type, and slip surfaces with little variation among each other are considered. A slip surface is considered to be composed of specific broken line segments. The unbalanced transfer coefficient method can be used for landslide stability calculation [26].

The unbalanced transfer coefficient method is based on the following four assumptions.

- The landslide body is considered as an incompressible body, and the extrusion deformation between the blocks is not considered in the calculation.
- Only the transfer of thrust is considered between blocks. A mutual transfer of tensile force, which is generally not considered in practical applications, and the specific tensile fracture situation between blocks are not considered in the calculation.
- The interblock force (i.e. thrust) is represented by a concentrated force, and its action line is parallel to the direction of the slip surface of the previous block.
- The basic section for the calculation is taken as the rock and soil body, with a unit length width perpendicular to the main axis of the landslide.

Considering *i* block as a separate body and decomposing each force in the direction of the slip surface of this block, the specific remaining sliding force of block i can be obtained E_i [12]:

$$E_i = W_i \sin\partial_i - W_i \cos\partial_i \tan\varphi_i - c_i l_i + \psi_i E_{i-1} \quad (8)$$

where:

E_i - the remaining sliding force of the *i*-th block of landslide body
E_{i-1} -the remaining sliding force of the (*i*-1)-th block of landslide body
W_i - weight of *i*-th block of landslide body
ψ_i - transfer coefficient, Eq (9)
c_i - cohesion of rock and soil on the slip surface of the *i*-th block of the landslide body.
l_i - length of slip surface of *i*-th block of landslide body
φ_i - internal friction angle of rock and soil on slip surface of *i*-th block of landslide
∂_i - inclination angle of slip surface of the *i*-th block of landslide body
$\partial_{(i-1)}$ - inclination angle of the slip surface of the (*i*-1)-th block of the landslide body.

$$\Psi_i = \cos(\partial_{i-1} - \partial_i) - \sin(\partial_{i-1} - \partial_i)\tan\varphi_i \quad (9)$$

If the value of the last soil mass E_n is such that the calculated value in the actual calculation is positive, the overall judgment of the landslide body is that it is an unstable soil mass; if it is negative or zero, it indicates that the rock mass is stable, and the calculation of the next block is carried out without considering the thrust of the previous block. The strength reduction finite unbalanced transfer coefficient method, that is, the strength reduction method of the slip-surface parameters, which is called in practical applications, simultaneously assigns a certain safety factor K to the slip-surface parameters tan φ_i and c_i for strength reduction to obtain the specific landslide sliding force under a certain safety factor. That is:

$$E_i = W_i \sin\partial_i - W_i \cos\partial_i \tan\varphi_i / k - c_i l_i / k + \psi_i E_{i-1} \quad (10)$$

In practical applications, the efficiency is relatively high when a finite method based on strength reduction is adopted. In particular, when the change in state of the slip-surface morphology in the front and rear sections is larger, the calculation results exhibit a greater difference [27]. The specific usage differences between the two methods are similar to the differences between the Swedish slice method and the simplified Bishop method, which are usually adopted in slope stability calculations in slope calculations. This is also the main reason why many specifications recommend a finite element method based on strength reduction in actual engineering. In practical applications, the use of a finite method based on strength reduction for slope stability analysis has further verified the corresponding good engineering effects [28].

Considering the use of the pseudostatic method, the seismic force was converted into a static force in the calculation, and the final form of the acting force was used in the landslide body calculation. Therefore, referring to soil dynamics, according to the "Code for Seismic Design of Railway Engineering" GB 50111-2019 [28], the rules for the use of the seismic angle under different seismic accelerations are listed in Table 12.

$$E_i = W_i \sin(\partial_i + \lambda) - W_i \cos(\partial_i + \lambda)\tan\varphi_i / k - c_i l_i / k + \psi_i E_{i-1} \quad (11)$$

Since the model in this study is above water and the maximum horizontal acceleration value is 0.3g in this experiment, the seismic angle λ is 4°30′, which is the value taken for the landslide in this experiment. If the value is considered for the thrust formula under a seismic force:

$$E_i = W_i \sin(\partial_i + 4°30') - W_i \cos(\partial_i + 4°30')\tan\varphi_i / k - c_i l_i / k + \psi_i E_{i-1} \quad (12)$$

6.2. Calculation of horizontal bearing capacity and displacement of anti-slide piles

According to the provisions of the Technical Code for Building Pile Foundations JGJ94-2018 (China) [30], when the pile

Table 12. Table of seismic angle values for different seismic accelerations

Peak ground acceleration value		0.1 g	0.2 g	0.3 g	0.4 g
Seismic angle	Above water	1° 30′	3°	4° 30′	7°
	Under water	2° 30′	5°	7° 30′	10°

Table 13. Maximum bending moment coefficient ν_M and horizontal displacement coefficient ν_x of the pile top (body)

Restraint conditions at the pile top	Converted embaded depth of the pile (α_h)	V_M	V_x
Hinged. free	4.0	0.768	2.441
	3.5	0.750	2.502
	3.0	0.703	2.727
	2.8	0.675	2.905
	2.6	0.639	3.163
	2.4	0.601	3.526
Note: h denotes the embedded length of a pile			

Table 14. 95 % confidence interval of embedded depth and pile-top displacement

Embedded depth	Pile top displacement	Lower confidence limit	Confidence upper limit
22	0.025	0.02	0.03
24	0.017	0.01	0.02
26	0.0102	0.01	0.01
28	0.0027	0.00	0.01

foundation in this experiment mainly bears horizontal forces, the calculation rule is that the interaction force between the pile and the soil, which mainly considers the group pile effect, can be specifically determined according to the following formula (13) as specified in the code:

$$x_{oa} = \frac{R_{ha} \cdot \nu_x}{a^3 \cdot EI} \tag{13}$$

where R_{ha} is the horizontal bearing capacity of a single pile, and after calculation

$$R_{ha} = \frac{1}{2} E_i \cos \partial_i \tag{14}$$

x_{0a} is the horizontal displacement at the pile top, ν_x is the horizontal displacement coefficient at the top of the pile, EI is the flexural rigidity of the pile body. For a reinforced concrete pile, $EI = 0{,}85E_cI_0$, where I_0 is the moment of inertia of the pile body's converted cross-section; for a rectangular cross-section, $I_0 = W_0b_0/2$; in this experiment, $I_0 = 4{,}17 \times 10^{-7}$, and E_c is the elastic modulus of reinforced concrete [19].

$$\alpha = \sqrt[5]{\frac{mb_0}{EI}} \tag{15}$$

In Eq (15) m is proportionality coefficient of the horizontal soil resistance coefficient of the pile side. According to the "Technical Code for Building Pile Foundations" JGJ94-2018 (China) [30], in this experiment, the value of m is 90. b_0 iscalculated width of the pile body (m). For a square pile: when the side width $b \leq 1$ m, $b_0 = 1{,}5b + 0{,}5$; in this experiment, $b_0 = 1{,}85$.

EI is flexural rigidity of the pile body. In this experiment, the horizontal displacement coefficient of the pile top $\nu_x = 2{,}441$, and the horizontal deformation coefficient of the pile $\alpha = 1{,}46$ [31]. Based on the above calculations, the horizontal displacement at the top of the pile is:

$$x_{0a} = 0{,}064E_i \cos \partial_i = 0{,}064W_i sin(\partial_i + 4°30') - \\ -W_i \cos(\partial_i + 4°30') \tan \varphi_i \div K - c_i l_i \div K + \psi_i E_{i-1}] \cos \partial_i \tag{16}$$

6.3. Formula for the embedded depth of anti-slide piles based on the transfer coefficient method

We analysed the seismic reinforcement effect of the embedded depth by taking the post-earthquake displacement and deformation amount at the time of soil arch failure as a sign. Because the embedded depths of 20 and 18 cm did not experience soil arch failure, we successively compared and analysed the soil arch failure time point at an embedded depth of 16 cm and the corresponding horizontal displacement at the pile top. The fitting analysis and the relational expressions obtained are presented in Figure 22.

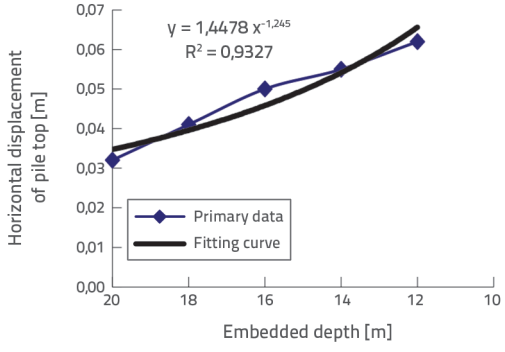

Figure 22. Relationship between embedment depth h and horizontal displacement of pile top

According to the physical experiments, the fitting range of h was 12–20 m, and the 95 % confidence intervals of the embedded depth and pile-top displacement are listed in Table 14. According to the physical experiments, the embedded depth h is given by:

$$h = 1.4478 x_{oa}^{-1.245} \tag{17}$$

Table 15. Units of physical quantities in expressions and their places of occurrence

Symbol	Name	Mjerna jedinica	Location of appearance
γ	Unit weight	kN/m³	P5, P5, P22
ρ	Density	kg/m³	P17
E	Elastic modulus	MPa or GPa	P22
ν	Poisson's ratio	Unitless.	P17, P22
c	Cohesion	kPa or MPa	P2, P4, P5, P6, P17, P22, P25, P28, P30, P34
φ	Angle of internal friction	°	P2, P4, P5, P6, P17, P22, P25, P28, P30, P34
FS	Factor of safety	Unitless.	P5, P26, P27
h	Penetration depth	m	P2, P27, P28, P29, P33, P34
IM	Strength index	Unitless.	P22

In summary, the final formula for determining the embedded depth of anti-slide piles is.

$$h = 1.4478\{0.064[W_i sin(\partial_i + 4°30') - W_i \cos(\partial_i + 4°30') \tan\varphi_i \div K - c_i l_i \div K + \psi_i E_{i-1}]\cos\partial_i\}^{-1.245}$$

7. Conclusion

Wet soil (small values of c and φ and large soil gravity) might not allow the anti-slide piles to perform their intended retaining function, and their construction was difficult and might not be economical. However, the dry soil was easily destroyed, and the seismic effect was poor. Notably, while controlling soil strength, other factors should be considered comprehensively to achieve the best engineering economic effect.

The failure and deformation processes of anti-slide pile-supported gravel-soil slopes under earthquake action were reproduced using indoor physical model tests. The seismic deformation distribution laws of the slopes differed at different embedment depths. When the embedment depth was relatively deep, or the soil strength was relatively large, the soil behind the pile did not slide, which might not allow the anti-slide pile to fully exert the retaining effect; construction was difficult and might not be economical. When the embedment depth was relatively shallow or the soil strength was relatively small, the deformation was intense from the beginning, indicating that the seismic resistance effect of the anti-slide pile was poor, and the supported slope was not very stable. Therefore, the study of the embedment depth of anti-slide piles is of great significance.

As the embedment depth increased, the earth pressure decreased. In particular, when the embedment depth was 12 cm (relatively shallow), the earth pressure was relatively high. When the embedment depths were 20 cm (relatively deep) or 16 cm (relatively appropriate), the earth pressures were similar. Within a certain embedment depth range, the earth pressure reached a certain value, and further increasing the embedment depth had little effect on the earth pressure.

Using a physical model test and numerical simulation data, combined with the strength reduction analysis method, a functional equation with a high fitting degree for the interaction between safety factor k and embedded depth h was summarised and established, considering the influence of factors such as gravel-soil slope and the interaction between piles and soil under earthquake load: $k = 0.0184h^{2.0108}$, where the parameter $R^2 = 0.9707$. The fitting formulas of internal friction angle φ, soil cohesion c, and embedding depth h in the embedded section were: $\varphi = 594.03h^{-1.419}$, where the parameter $R^2 = 0.9773$, and $c = 14366h^{-2.13}$, where the parameter $R^2 = 0.9878$.

The influence of earthquakes on the dynamic response of anti-slide pile-supported gravel soil slopes under different embedment depths and soil strengths was analysed. Relevant research on the embedment depth of anti-slide piles was conducted based on the strength reduction unbalanced transfer coefficient method. Through the selected gravel-soil landslide, the influence of the soil strength on the embedded section was studied, and the optimal embedment depth of the anti-slide piles in soils with different strengths under certain landslide thrust conditions was determined. Furthermore, an empirical discriminant formula was established for the optimal embedment depth of anti-slide piles in gravel soil as follows:

It further revealed the specific impacts of many sensitive factors, such as the embedment depth, soil water content, and pile-soil properties, on the distribution mode of external loads, improved the understanding of the response law, and provided a theoretical basis and relevant scientific guiding suggestions for explaining the force mechanism of its support system and research on the specific embedment depth. Eventually, it was expected to provide a corresponding theoretical basis and relevant scientific guidance suggestions.

REFERENCES

[1] Kong, J., Fayou, A., Wenping, W.: Analysis of landslide types and typical cases in Wenchuan earthquake, Journal of Soil and Water Conservation (China), 23 (2009) 6, pp. 66-70, https://doi.org/103321/j.issn:1009-2242.2009.06.016

[2] Hungr, O.: The Varnes Classification of Landslide Types, an Update, Landslides, 11 (2014) 2, pp 167-194, https://doi.org/10.1007/s10346-013-0436-y

[3] Bačić, M., Librić, L., Ivšić, T.: Estimation of the bored pile capacity and settlement in soft soil, GRAĐEVINAR, 65 (2013) 10, pp. 901-918, https://doi.org/10.14256/JCE.912.2013

[4] Li, G.J., Motamed, R.: Finite Element Modeling of Soil-Pile Response Subjected to Liquefaction-Induced Lateral Spreading in a Large-Scale Shake Table Experiment, Soil Dynamics and Earthquake Engineering, 92 (2017), pp. 573-584, https://doi.org/10.1016/j.soildyn.2016.11.001

[5] Zhang, J., Li, Y.R., Rong, X., Liang, Y.: Dynamic p-y Curves for Vertical and Batter Pile Groups in Liquefied Sand, Earthquake Engineering and Engineering Vibration, 21 (2022) 3, pp. 605-616, https://doi.org/10.1007/s11803-022-2107-2

[6] Zhang, J., Li, Y.R., Yan, Z.X., Huang, D., Rong, X., Liang, Y.: Experimental Study of Vertical and Batter Pile Groups in Saturated Sand Using a Centrifuge Shaking Table, Earthquake Engineering and Engineering Vibration, 21 (2022) 1, pp. 23-36. https://doi.org/10.1007/s11803- 021-2067-y

[7] Zhang, X.R., Yang, Z.J.: Numerical Analyses of Pile Performance in Laterally Spreading Frozen Ground Crust Overlying Liquefiable Soils, Earthquake Engineering and Engineering Vibration, 17 (2018) 3, pp. 491-499. https://doi.org/10.1007/s11803-018-0457-6

[8] Türedi, Y., Örnek, M.: Analysis of model helical piles subjected to axial compression, GRAĐEVINAR, 72 (2020) 9, pp. 759-769, https://doi.org/10.14256/JCE.2660.2019

[9] Tang, L., Maula, B.H., Ling, X.Z., Su, L.: Numerical Simulations of Shake-Table Experiment for Dynamic Soil-Pile-Structure Interaction in Liquefiable Soils, Earthquake Engineering and Engineering Vibration, 13 (2014) 1, pp. 171-180, https://doi.org/10.1007/ s11803-014-0221-53

[10] Vukićević, M., Marjanović, M., Pujević, V., Nikola. O,: Evaluation of methods for predicting axial capacity of jacked-in and driven piles in cohesive soils, GRAĐEVINAR, 70 (2018) 8, pp. 685-693, https://doi.org/10.14256/JCE.2175.2017

[11] Li, J.B., Zhang, H.R., Li, Z.Q.: Theoretical Study on Similarity Relation of Small Scale Subgrade Shaking Table Test Model. Advanced Materials Research, 255-260 (2011), pp. 3354-3360, https://doi.org/10.4028/www.scientific.net/AMR.255-260.3354

[12] Mansoujian, M.R., Ghomeshi, M., Hasounizadeh, H., Hosseini, S.A.: Effects of cylindrical and cubic piles on motion of density currents, GRAĐEVINAR, 73 (2021) 5, pp. 499-507, https://doi.org/10.14256/JCE.2867.2019

[13] Shen, D.J., Lu, X.L.: Experimental Study on the Mechanical Property of Microconcrete in Model Test, China Civil Engineering Journal, 43 (2010) 10, pp. 14-21, (In Chinese) https://doi.org/10.15951/j.tmgcxb.2010.10.013.

[14] Li, R.: Design of the microconcrete anti-sliding model pile in the dynamic centrifugal model test. Journal of Tsinghua University (China), 49 (2009) 9, pp. 66-70, (China), https://doi.org/ 10.3321/j.issn:1000-0054.2009.09.017

[15] Zou, Z.Y., Lei, D., Jiang, G.L., Luo, B., Chang, S.Z., Hou, C.P.: Experimental Study of Bridge Foundation Reinforced with Front and Back Rows of Anti-Slide Piles on Gravel Soil Slope Under El Centro Waves, Applied Sciences, 10 (2020) 9, pp. Paper No. 3108, https://doi.org/10.3390/app10093108

[16] Sokolić, I., Kereš, B.: Experience in execution of driven reinforced concrete piles in Croatia, GRAĐEVINAR, 77 (2025) 6, pp. 593-603, https://doi.org/10.14256/JCE.4253.2025

[17] Lin, Y.L., Cheng, X.M., Yang, G.L. Shaking Table Test and Numerical Simulation on a Combined Retaining Structure Response to Earthquake Loading, Soil Dynamics and Earthquake Engineering, 108 (2018), pp. 29- 45, https://doi.org/10.1016/j.soildyn.2018.02.008

[18] Zou, Z.Y., Lei, D., Jiang, G.L., Luo, B., Chang, S.Z., Hou, C.P.: Experimental Study of Bridge Foundation Reinforced with Front and Back Rows of Anti-Slide Piles on Gravel Soil Slope Under El Centro Waves, Applied Sciences, 10 (2020) 9, Paper 3108, https://doi.org/10.3390/ app1009310

[19] Martin, G.R., Chen, C.Y.: Response of Piles due to Lateral Slope Movement, Computers and Structures, 83 (2005) 1, pp. 588-598, https://doi.org/10.1016/j. compstruc.2004.11.006

[20] Nian, T.K., Chen, G.Q., Luan, M.T., Yang, Q., Zheng, D.F.: Limit Analysis of the Stability of Slopes Reinforced with Piles Against Landslide in Nonhomogeneous and Anisotropic Soils, Canadian Geotechnical Journal, 45 (2008) 8, pp. 1092-1103, https://doi.org/10.1139/T08-042

[21] Shukla, R.P.: Pile groups subjected to abrupt collapse of retaining structure, GRAĐEVINAR, 70 (2018) 11, pp. 953-964, https://doi.org/10.14256/JCE.1626.2016

[22] Martin, G.R., Chen, C.Y.: Response of Piles due to Lateral Slope Movement, Computers and Structures, 83 (2005) 1, pp. 588-598, https://doi.org/10.1016

[23] Guo, J.Q., Xi, W.F., Yang, Z.Q., et al.: Landslide hazard susceptibility evaluation based on SBAS-InSAR technology and SSA-BP neural network algorithm: A case study of the Baihetan Reservoir Area, J Mt Sci, 21 (2024), pp. 952-972, https://doi.org/10.1007/s11629-023-8083-9

[24] Wang, J.D., Zhang, D.F., Wang, N.Q., et al.: Mechanisms of wetting-induced loess slope failures, Landslides, 16 (2019), pp. 937-953, https://doi.org/10.1007/s10346-019-01144-4

[25] Yang, S., Leshchinsky, B., Cui, K., Zhang, F., Gao, Y.: Influence of Failure Mechanism on Seismic Bearing Capacity Factors for Shallow Foundations Near Slopes, Géotechnique, 0 (0), pp. 1-14. http://doi.org/10.1680/ jgeot.19.P.329

[26] Zhou, D.P., Xiao, S.G., Xia, X.: Discussion on Rational Spacing Between Adjacent Anti-Slide Piles in Some Cutting Slope Projects, Chinese Journal of Geotechnical Engineering, 26 (2004) 1, pp. 132-135, https://doi.org/10.1007/BF02911033.

[27] Ministry of Transport, People's Republic of China: Code for Seismic Design of Highway Engineering (JTG/T 2231 - 01-2020)(China), Beijing: China Communications Press, 2020.

[28] Ministry of Construction of the People's Republic of China: Code for Seismic Design of Railway Engineering (GB 50111-2019), Beijing: China Railway Publishing House. 2022.

[29] Liang, R., Zeng, S.: Numerical Study on Soil Arching Mechanism in Drilled Shafts for Slope Stabilization, Soil and Foundation, 42 (2002) 2, pp. 83-92, https://doi.org/10.3208/sandf.42.2_83

[30] Ministry of Construction, People's Republic of China: Technical Code for Building Pile Foundations (JGJ 94-2018), Beijing: China Architecture and Building Press, 2021

[31] Nian, T.K., Chen, G.Q., Luan, M.T., Yang, Q., Zheng, D.F.: Limit Analysis of the Stability of Slopes Reinforced with Piles Against Landslide in Nonhomogeneous and Anisotropic Soils, Canadian Geotechnical Journal, 45 (2008) 8, pp. 1092-1103, https://doi.org/10.1139/T08-042